electronics

MDPI

Article

On the Asymmetry of Resistive Switching Transitions

Guillermo Vinuesa [1,*], Héctor García [1], Eduardo Pérez [2,3], Christian Wenger [2,3], Ignacio Íñiguez-de-la-Torre [4], Tomás González [4], Salvador Dueñas [1] and Helena Castán [1]

1 Department of Electronics, Universidad de Valladolid, Paseo de Belén 15, 47011 Valladolid, Spain; hecgar@ele.uva.es (H.G.); sduenas@ele.uva.es (S.D.); helena@ele.uva.es (H.C.)
2 IHP-Leibniz-Institut für Innovative Mikroelektronik, 15236 Frankfurt (Oder), Germany; perez@ihp-microelectronics.com (E.P.); wenger@ihp-microelectronics.com (C.W.)
3 Faculty 1 MINT-Mathematics, Computer Science, Physics, Electrical Engineering, and Information Technology, BTU Cottbus-Senftenberg, 03046 Cottbus, Germany
4 Applied Physics Department and NANOLAB USAL, Universidad de Salamanca, Plaza de la Merced s/n, 37008 Salamanca, Spain; indy@usal.es (I.Í.-d.-l.-T.); tomasg@usal.es (T.G.)
* Correspondence: guillermo.vinuesa@uva.es

Abstract: In this study, the resistive switching phenomena in TiN/Ti/HfO_2/Ti metal–insulator–metal stacks is investigated, mainly focusing on the analysis of set and reset transitions. The electrical measurements in a wide temperature range reveal that the switching transitions require less voltage (and thus, less energy) as temperature rises, with the reset process being much more temperature sensitive. The main conduction mechanism in both resistance states is Space-charge-limited Conduction, but the high conductivity state also shows Schottky emission, explaining its temperature dependence. Moreover, the temporal evolution of these transitions reveals clear differences between them, as their current transient response is completely different. While the set is sudden, the reset process development is clearly non-linear, closely resembling a sigmoid function. This asymmetry between switching processes is of extreme importance in the manipulation and control of the multi-level characteristics and has clear implications in the possible applications of resistive switching devices in neuromorphic computing.

Keywords: resistive switching; RRAM; memristor; transient; temperature dependence; low power consumption

Citation: Vinuesa, G.; García, H.; Pérez, E.; Wenger, C.; Íñiguez-de-la-Torre, I.; González, T.; Dueñas, S.; Castán, H. On the Asymmetry of Resistive Switching Transitions. *Electronics* **2024**, *13*, 2639. https://doi.org/10.3390/electronics13132639

Academic Editors: Daniel Arumí and Salvador Manich

Received: 11 June 2024
Revised: 27 June 2024
Accepted: 2 July 2024
Published: 5 July 2024

1. Introduction

Resistive Random-Access Memory (RRAM) devices based on the resistive switching (RS) effect have been receiving increased interest recently. Positioned as potential successors to conventional memory technologies such as SRAM or DRAM, RRAM devices are especially relevant due to their properties: ultrafast switching operation, low power consumption, CMOS compatibility and great scalability, as well as simple device structure (metal–insulator–metal or MIM) [1–3]. Moreover, they have prospective applications in hardware encryption [4] and, most importantly, in neuromorphic computing [5,6].

The RS phenomenon is very well documented. First, an electroforming process must be carried out, in which a conductive filament (or several filaments) is formed for the first time through the dielectric, short-circuiting the metal electrodes. Then, one can partially disrupt this filament through the reset process, arriving at the high-resistance state (HRS), and then form it again (set transition) [7,8], returning to a low-resistance state (LRS). This process is reversible and non-volatile, as the device will maintain the last achieved resistance state [7]. Resistive switching can be either unipolar (URS) or bipolar (BRS), and there are several physical mechanisms that may be responsible for the creation of the conductive filament (CF) [9,10]. However, in BRS HfO_2-based MIM devices, when none of the metal electrodes are electrochemically active, the BRS is usually based on the Valence Change

Mechanism, which means that the CF is formed by oxygen vacancies and the conduction mechanism is based on electron hopping through vacancy-rich dielectric regions [11,12].

Another relevant property of RRAM devices is the ability to acquire several resistance states that are between the LRS and HRS [13,14], which, theoretically, are as stable as the low- and high-resistance states. These multilevel properties make RRAM devices able to emulate neuronal synapses by simulating synaptic weights, which is of extreme importance for neuromorphic computing [13–15].

In order to control these intermediate states, an accurate understanding of the set and reset processes is crucial, as these are the mechanisms by which we can change the resistance state. To this end, previous authors have studied the dynamics of resistive switching by changing voltage ramp rates [16–19]. These studies demonstrate that, as the ramp rate rises, both switching voltages increase. The asymmetry of the resistive switching transitions has also been previously observed, with studies usually focusing on the fact that the set transition is much faster than the reset. This has been attributed to electron trapping/detrapping occurring during the set and drift of oxygen vacancies in the reset [20], asymmetric redox reactions for each switching transition [21], different internal electric fields driving oxygen vacancy migration across the tunnel barrier interface for each process [22] and electron screening in the set process being faster than for oxygen vacancies [23].

In this work, we intend to expand the understanding on the dynamics of resistive switching, focusing on the switching processes of RRAM devices and their differences. For this purpose, we have investigated the potential differences in the conduction mechanisms that govern the LRS and HRS states, from which the set and reset processes are initiated. Thus, we conducted measurements over a wide temperature range. Additionally, we measured the temporal evolution of both processes by obtaining current transients at room temperature, with the aim of studying the distinction between the set and reset processes.

2. Materials and Methods

The samples characterized in this work (see Figure 1) are MIM devices placed on top of metal 2 of the 130 nm CMOS process. They are based on a TiN/Ti/HfO_2/TiN stack. The three metallic layers are deposited by magnetron sputtering. The top and bottom TiN electrodes are 150 nm thick, while the scavenging Ti layer is 7 nm thick. The dielectric HfO_2 layer was grown by atomic layer deposition (ALD) with a thickness of 8 nm. The area of each MIM device is 600×600 nm^2. The endurance of these samples has been previously studied and found to be of at least 1000 cycles [24]. In that study, it can be seen that the main trade-off of the low power consumption of these devices is their variability. Additionally, very similar samples with HfO_2 slightly doped with aluminum (10% aluminum content) have shown an endurance of 200,000 cycles when using pulses, a retention of over 10 years at low temperatures (<100 °C) [25] and switching speeds of 50 ns [26].

Electrical measurements were made by means of a Keithley 4200-SCS semiconductor parameter analyzer (Tektronix, Beaverton, OR, USA), with the samples put on a light-tight probe station. I–V curves were carried out in a wide (40–340 K) temperature range using a LakeShore CRX-VF (Lake Shore Cryotronics, Westerville, OH, USA) cryogenic probe station. Continuously variable temperature (CVT) probes allowed us to measure through temperature sweeps without the need to lift and re-land the probes each time the temperature was adjusted, improving reliability, avoiding damage of the pads and enabling automation. Current transients were performed by applying a constant voltage capable of initiating the set or reset voltage, measuring the current as fast as the equipment–computer communication allowed. The transients were obtained at room temperature with the help of a Hewlett-Packard 4155B semiconductor parameter analyzer (Hewlett Packard, Palo Alto, CA, USA) connected to a computer via GPIB and controlled with the Keysight VEE Education 9.32 software. The HP 4155B measures current with an accuracy of 0.12%, except when the current values are below 10 nA, where the accuracy drops to 0.5%.

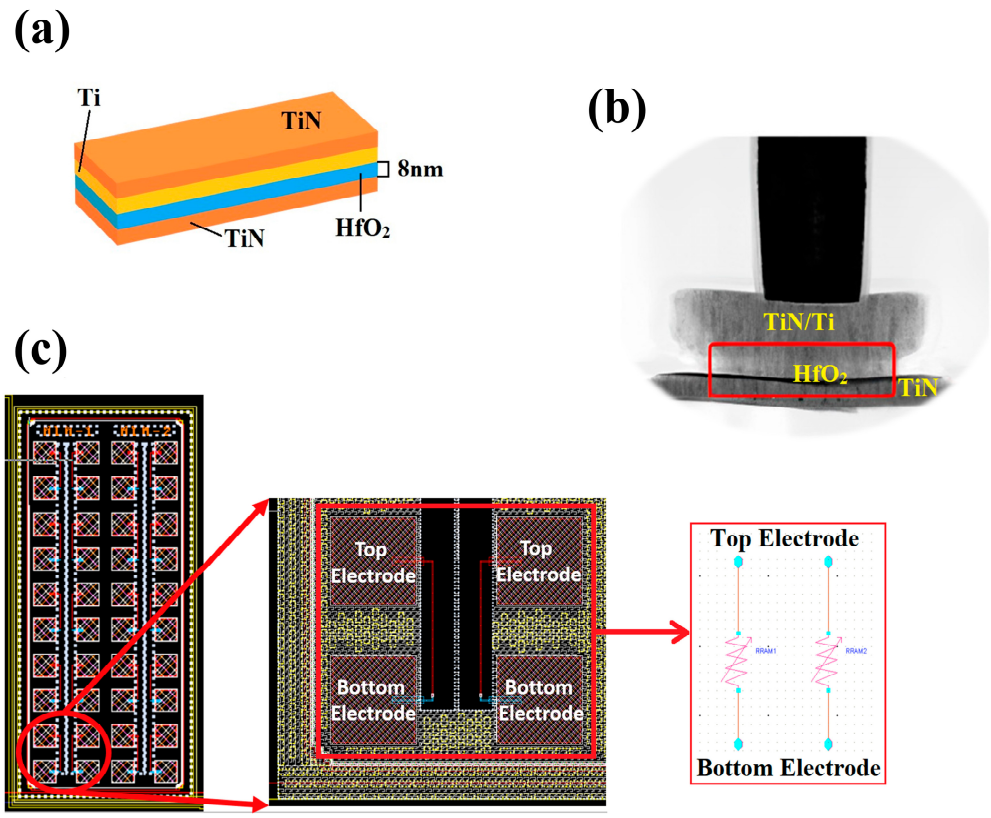

Figure 1. (**a**) Schematic of the cross-section of the TiN/Ti/HfO_2/TiN MIM stack. (**b**) TEM inspection. (**c**) Optical image and schematic of the memory device.

3. Results and Discussion

TiN/Ti/HfO_2/TiN devices showed excellent and repetitive resistive switching properties at room temperature (Figure 2a). More importantly, these devices show very low power consumption, as both LRS and HRS remain in the microamperes range and maximum and minimum voltages values remain in the [−1 V, 0.7 V] range, with the calculated power consumption always being below 250 µW during the resistive switching I–V loop (Figure 2b). This is especially interesting for the plausible memory applications expected of these devices (see Section 1. Introduction), as the switching between states can not only be made very fast but also at low power. Nevertheless, it is also readily apparent that there is great variability in switching voltages (especially in the set voltage) within the previously mentioned voltage range. Already at room temperature, a difference between switching transitions can be observed. While the set process is sudden, leading to an abrupt change in the current value, the reset process seems to be much more gradual. We will now study this difference in switching transitions by examining the effect of the temperature as well as the temporal evolution of both processes, with the intention of understanding the underlying physics or the reasons behind these differences.

Turning to the temperature measurements, it can be seen in Figure 3a that the studied samples showed the resistive switching effect in all temperature ranges, with the temperature going as low as 40 K. The RS remained repetitive at all temperatures, with 10 I–V cycles being made at each temperature (average curves can be seen in Figure 3b). A statistical analysis made through box plots in Figure 3c allows us to determine that, indeed, temperature affects the switching voltages. The absolute value of both set and reset voltages decreases when temperature increases, with this effect being much more noticeable in the reset process. The decrease in switching voltages can be directly linked to the temperature through the thermal energy of oxygen vacancies. As the temperature decreases, the energy needed for oxygen vacancies and ions to be able to move increases [27], leading to a need for higher voltages. Moreover, looking at the box plots shown in Figure 3d, it can be seen

that the LRS current increases as temperature rises. A higher current inevitably leads to a higher temperature in the CF through Joule heating, which accelerates the reset process at higher temperatures (thus resulting in a need for lower reset voltages). This can also be the explanation behind the fact that the reduction in voltage is much more apparent in the reset process, as the current in the HRS does not appear to be temperature-dependent, leading to a lesser reduction in set voltages when compared to the reset process.

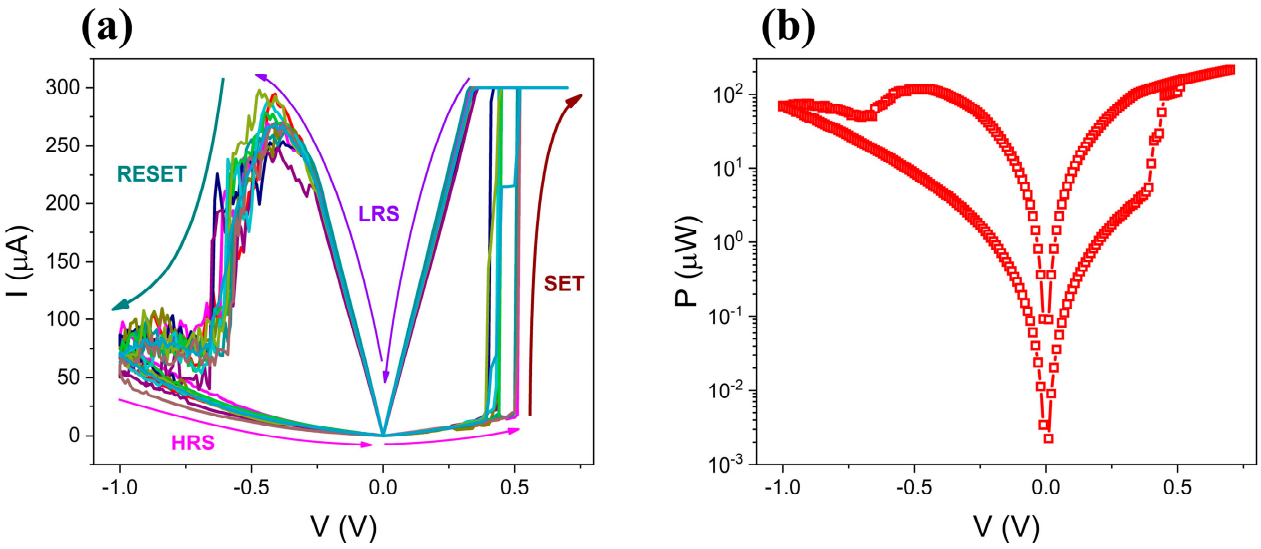

Figure 2. (**a**) I–V curves (10 cycles) of the TiN/Ti/HfO_2/TiN devices at room temperature. (**b**) Power consumed in the TiN/Ti/HfO_2/TiN devices during the RS effect. The power was calculated based on the voltage applied and current recorded in Figure 2a.

Nevertheless, to understand the temperature effect on the resistive switching properties previously discussed, we must use the temperature measurements to determine the main conduction mechanisms both in the low- and high-resistance states. In this case, analyzing the HRS is easier, as there is no clear temperature dependence of the resistance. Usually, a non-thermal effect leads to tunneling mechanisms in the high-resistance state. However, in this case, the HRS's current does not follow neither the Fowler–Nordheim $\left(\ln\left(\frac{I}{V^2}\right) \propto V^{-1}\right)$ nor the Trap-assisted Tunneling $\left(\ln(I) \propto V^{-1}\right)$ mechanisms [28,29]. Rather, the main conduction mechanism is proved to be Space-charge-limited Conduction (SCLC), as it can be easily identified by two regions (Figure 4a), with the I–V characteristics following the ohmic law $(I \propto V)$ at low voltage, followed by a power law (also known as Child's law $\left(I \propto V^2\right)$). In the first region, the conduction is dominated by the thermally generated free electrons in the insulator film, while the electrode-injected electrons dominate the conduction in the second region [29]. Although Figure 4a may give the impression that the I–V response is somewhat affected by the temperature, it must be noted that there is no clear tendency and that HRS variability is high, as it can be seen on the cycles plotted in Figure 3a and the box plot of Figure 3d. This can also be assessed by the fact that the thermal effect on the I–V response is not the same depending on the cycle used, which is illustrated in Figure 4 by making a comparison between the average cycle (Figure 4a) and the most representative cycle (Figure 4b). By "most representative cycle", we intended to convey the mode, which is the most frequently occurring value. Given the small number of cycles (only ten) for statistical analysis, we chose the cycle that most frequently matched other cycles in terms of set and reset voltages and similar current values. Thus, it is seen that mean and mode do not show the same thermal dependency due to resistance state variability.

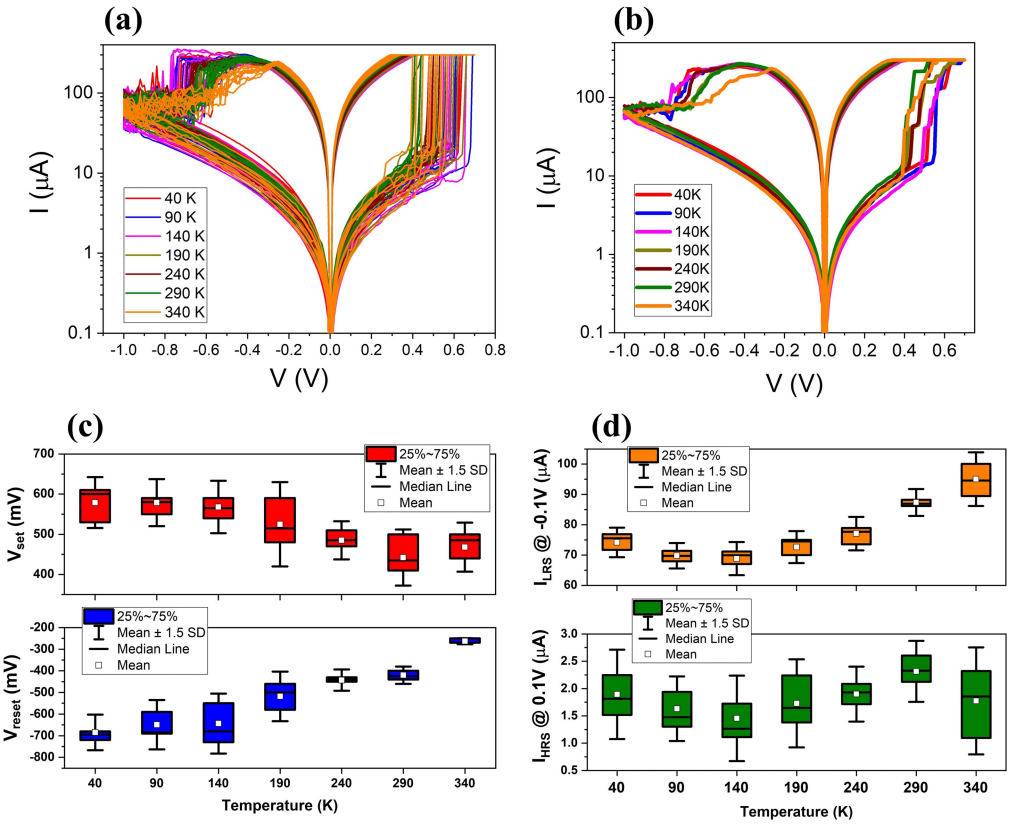

Figure 3. (**a**) I–V curves (10 cycles) and (**b**) average I–V curves at each temperature in the 40–340 K range. Box plots of (**c**) set and reset voltages as well as (**d**) current values in the HRS and LRS (measured at 0.1 V) at every temperature.

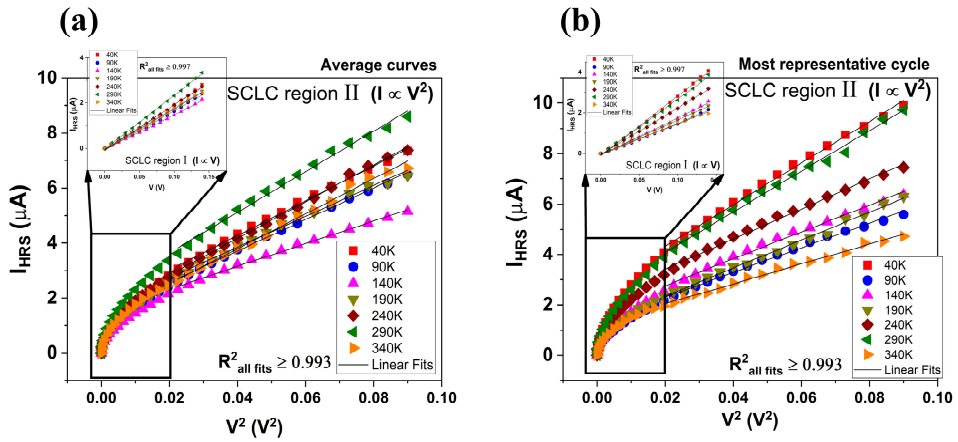

Figure 4. Space-charge-limited conduction plot of I_{HRS} vs. V^2 at every temperature. Insets: ohmic plot representing region (i) of the SCLC mechanism. (**a**) Average curves and (**b**) most representative cycle at each temperature.

Among previously published works, it is usual that, when the SCLC mechanism rules the HRS, the same behavior is seen in the LRS [29–33], although there are some exceptions [34,35]. Indeed, as it is shown in Figure 5, we can again identify the two regions that indicate SCLC in the LRS: first the ohmic law at low voltages and then the power law as the applied electric field increases. Nevertheless, we can see that there is a tendency, with the current increasing as the temperature rises, at least in the 140 K and 340 K range, which can also be seen in the box plot of Figure 3d. This can be explained by another conduction mechanism, which could play a role along the SCLC. Among the several temperature-dependent mechanisms, only Schottky (thermionic) emission fitted

both voltage and temperature dependencies (see Figure 5), with other mechanisms such as Ionic, Ohmic, Poole-Frenkel, Nearest Neighbor and Variable Range Hopping being discarded.

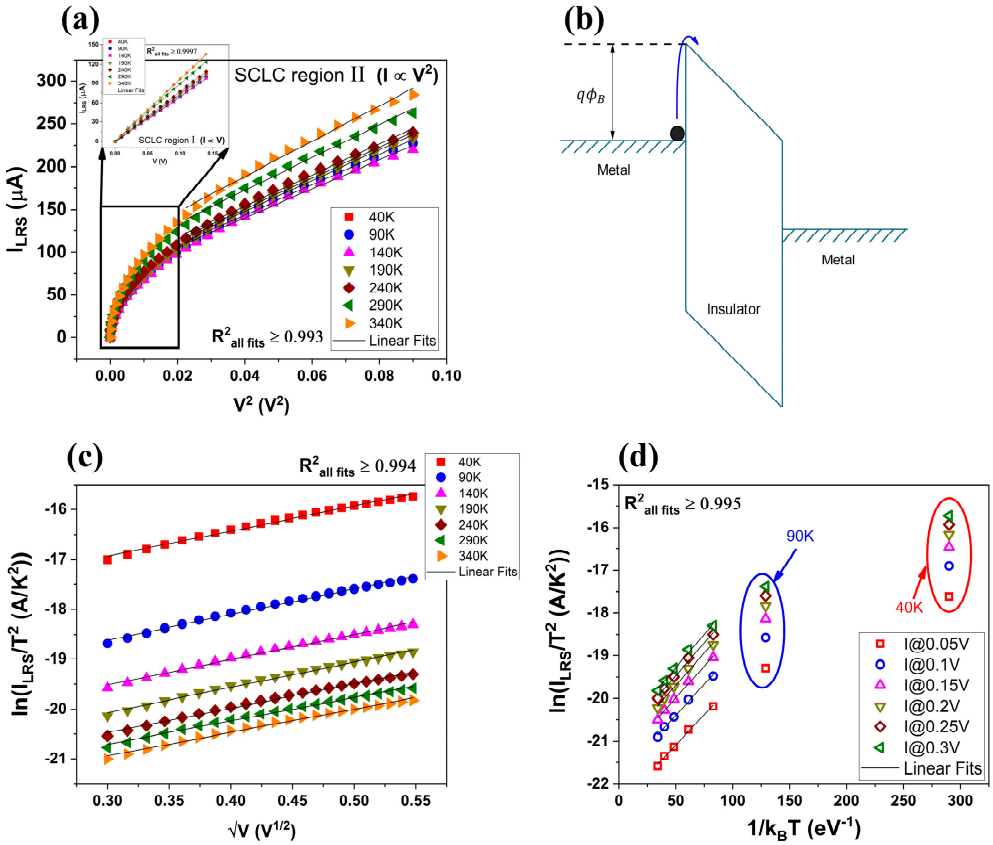

Figure 5. (**a**) Space-charge-limited conduction plot of I_{LRS} vs. V^2 at every temperature. Inset: ohmic plot representing region (i) of the SCLC mechanism. (**b**) Schematic energy band diagram of Schottky emission in MIM structures. (**c**) Schottky emission plot against voltage $\left(\ln\left(\frac{I_{LRS}}{T^2}\right) \propto \sqrt{V}\right)$ and (**d**) temperature $\left(\ln\left(\frac{I_{LRS}}{T^2}\right) \propto \frac{1}{k_B T}\right)$. All plots use the average curves of Figure 3b.

Now, taking into account that the CF is partially disrupted when our device is in the HRS, it makes sense that we are also able to see another conduction mechanism in the LRS. When the filament is broken, the potential barrier is too great to even see it, as electrons must travel not only through the CF but also through the dielectric before arriving at the metal electrode. Meanwhile, in the LRS, both metal electrodes are short-circuited by the CF. This means that the potential barrier needed to be surpassed by the electrons is much smaller and we are able to observe it through the temperature dependence that characterizes the Schottky emission mechanism.

This marks yet another asymmetry between set and reset transitions. While the set process starts in the HRS, governed only by the SCLC, the LRS, which presents both SCLC and Schottky emission, gives birth to the reset transition. As we mentioned when analyzing the I–V curves at room temperature, it is clear that in the set process, once the electric field needed to form the CF is applied, the transition occurs in an instant. Meanwhile, the reset starts slowly and then the filament starts to dissolve increasingly faster. This may be related to the fact that, in the reset process, as we are in the LRS, electrons are able to move more freely, which in turn provokes Joule heating, which is ultimately the trigger of the reset process. Increasing the voltage then leads to the recombination of oxygen ions and vacancies, starting the disruption of the CF. On the other hand, for the set process, we need to be able to move the oxygen ions to the Ti cap that acts as an oxygen reservoir [31–38], leaving oxygen vacancies behind, which seems to occur once certain

applied voltage is reached. Indeed, looking at the current transients of both set and reset transitions in Figure 6, we can clearly observe what has just been discussed, while the set process presents an almost linear relationship with the logarithm of time after a sudden increase in current value, the reset process resembles a sigmoidal function, presenting three regions, where the first and last are much slower than the intermediate one, which, although not as fast as the set process, shows a fast decrease in current value.

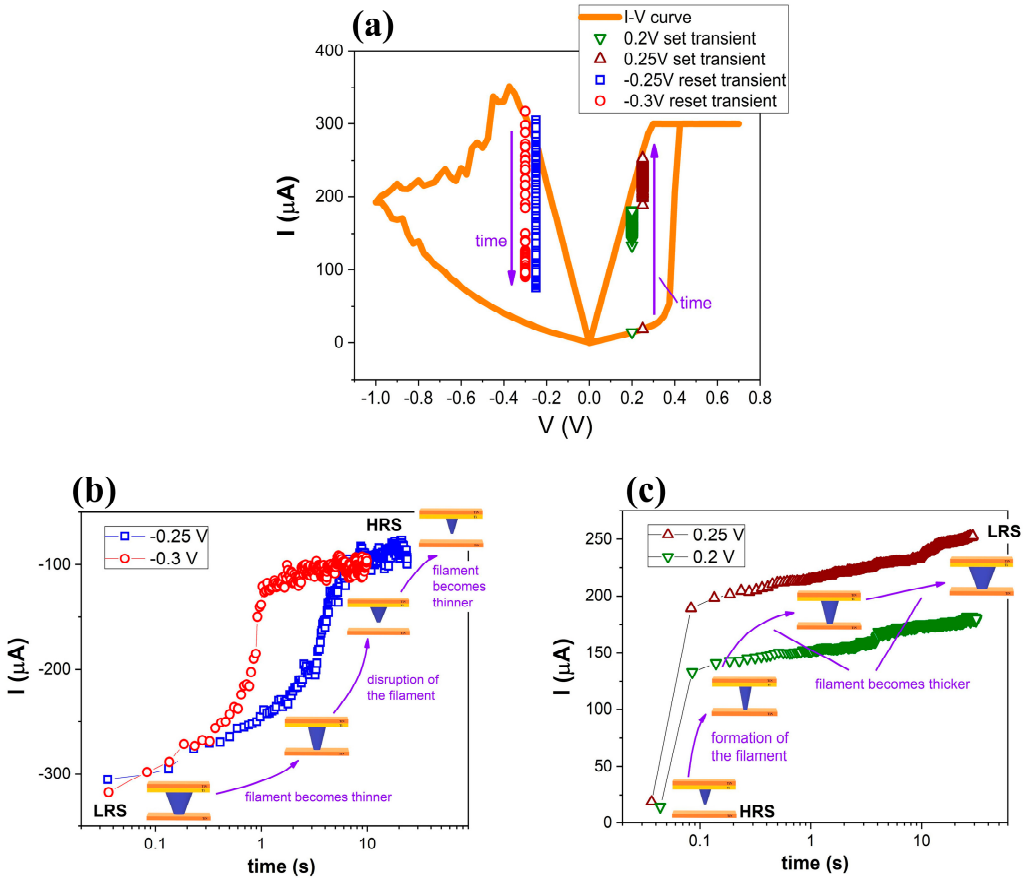

Figure 6. (**a**) I–V curve of a TiN/Ti/HfO_2/TiN sample at room temperature with two set and two reset transients. (**b**) Reset current transients and CF evolution vs. time and (**c**) set current transients and CF evolution against time.

These results show great consistency with the filamentary model presented in [39], which describes the evolution of the conductive filament (CF) geometry during resistive switching (RS). The CF, shaped like a truncated cone, changes in volume based on the gap (space between CF tip and metal electrode) and CF radius. This model is closely reproduced in the CF evolution depicted among the transients in Figure 6b,c, which we will describe along with our experimental measurements hereunder.

During the set process, the instant increase in current is explained by the filament short-circuiting the metal electrodes through the dielectric layer (that is, in the CF model of [39], the gap reaches its minimum value). As we apply a positive voltage, oxygen ions (O_2^-) migrate to the top electrode, and this generates oxygen vacancies in the dielectric layer that form the CF, short-circuiting the metal electrodes [10]. After that, by applying more voltage, we are able to generate more vacancies, essentially thickening the already formed filament (CF radii, both top and bottom, increase), which can be seen in the linear increment of current with the logarithm of time. On the other hand, the reset process does not start with the disruption of the CF, hence why a sudden decrease in current is not observed. Rather, a slow but steady decrease in current is measured first, which indicates an initial recombination of oxygen ions (that now travel towards the bottom electrode as

we apply negative voltage) and vacancies that slim the filament down (CF top and bottom radii decrease). Then, as the applied voltage increases, the recombination process speeds up, disrupting the CF and leading to a much faster decrease in current (the gap reaches its maximum value). Finally, we can observe how the decrease in the current value slows down again, which may be because the length of the broken CF arrives at a somewhat stable configuration, but the recombination still exists, which allows the filament to thin. This last part of the reset process may also be explained by the fact that, although by applying more negative voltage we break the CF more, we also facilitate the movement of electrons, which increases the value of the current. It can be considered that in both the set and reset processes, the main species that move are the oxygen ions, which essentially leave immobile oxygen vacancies behind them in the set process, with which they recombine later during the reset transition [40].

Taking these results into account, it is clear that the reset process is slower than the set transition and, thus, much more easily controlled, also in terms of the multi-level capabilities of the sample. This can be seen in previously published studies, where authors obtain several more intermediate states during the reset, when compared to the set [41]. This is in direct relation with the fact that the switching transitions respond differently to electric stimuli. The reset is easily controlled via voltage, while the set process is more accurately controlled by applying current, as it allows for a smooth transition and removes the need for current compliance. In contrast, the reset is abrupt and needs a voltage compliance when using current, which implies that we should use different magnitudes to accurately control the intermediate states in each transition [42]. Moreover, not only does the reset process require more time than the set transition, but, as shown in Figure 7, it also consumes more power, which highlights another asymmetry between the resistive switching processes. This implies that not only do we need more time to dissolve the CF but we also need to consume more power to do so, as, according to the previously described filamentary model, in order to disrupt the CF, we must first be able to "thin" it, which occurs in the first part of the transient, where the current/power slowly decrease in value before the drop that marks the breaking of the filament. These asymmetries are crucial when optimizing the performance of RRAM devices, such as their power consumption and switching speeds or controlling the desired resistance states.

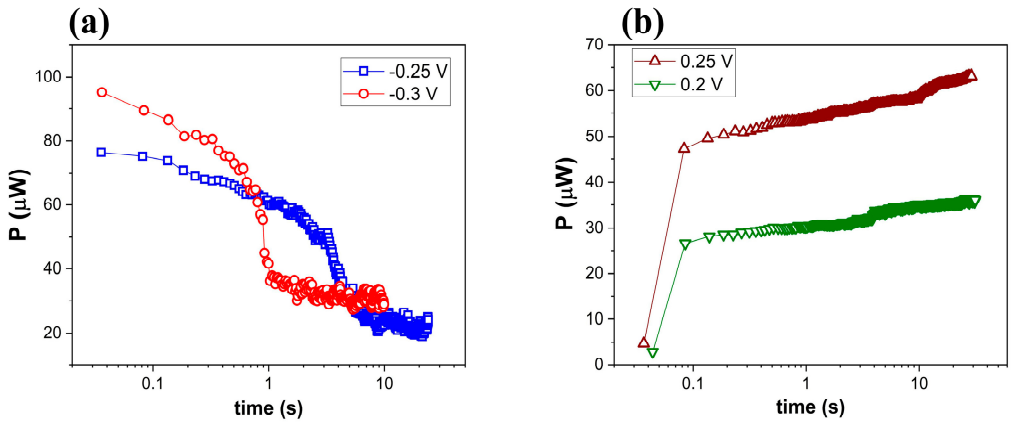

Figure 7. (**a**) Reset power transients. (**b**) Set power transients.

4. Conclusions

Switching transitions are fundamentally different processes, and thus, their I–V characteristics are asymmetric. Both low- and high-resistance states' main conduction mechanism is space-charge-limited conduction, but Schottky emissions are found alongside the SCLC in the LRS, explaining its thermal dependence. This marks the first physical difference between set and reset, as it implies that, in the LRS, the current is greater at higher temperatures, leading to Joule heating, and thus, the reset occurs at lower voltages. The temporal evolution of both transitions is also different; while the set process occurs almost instantly,

the reset is slower, showing three distinct regions that resemble a sigmoid function. This can be explained by the sudden creation of the filament in the set process and its subsequent thickening, while the reset process starts with the filament "thinning", leading to a slow and steady decrease in current until a certain voltage, which enables filament disruption, is reached, showing a faster decline in current values. The third and slower region is explained by a struggle marked by the growing negative voltage, which favors the movement of electrons while also breaking the filament, destroying their conductive paths. Finally, not only is the reset process slower than the set transition but it also consumes more power.

Further research is needed to explore the dynamics of resistive switching. To do this, pulsed measurements and transient measurements over a broad temperature range may be especially interesting. Additionally, more effort should be made to define a compact mathematical model to describe the temporal evolution of the switching processes.

Author Contributions: Conceptualization, G.V. and H.C.; methodology, G.V., H.G., S.D. and H.C.; software, H.G.; validation, S.D. and H.C.; formal analysis, G.V.; investigation, G.V.; resources, S.D., H.C., E.P., C.W., I.Í.-d.-l.-T. and T.G.; data curation, G.V.; writing—original draft preparation, G.V.; writing—review and editing, H.C. and E.P.; visualization, G.V. and E.P.; supervision, H.C., C.W. and I.Í.-d.-l.-T.; project administration, S.D., H.C., T.G., I.Í.-d.-l.-T. and C.W.; funding acquisition, S.D., H.C., T.G., I.Í.-d.-l.-T., E.P. and C.W. All authors have read and agreed to the published version of the manuscript.

Funding: We acknowledge grant PID2022-139586NB-C43 funded by MCIN/AEI/10.13039/501100011033 and by ERDF A way of making Europe. USal authors thank grant PID2020-115842RB-I00 funded by MCIN/AEI/10.13039/501100011033 and the Junta de Castilla y León and FEDER through project SA136P23. IHP authors would like to thank the German Federal Ministry of Education and Research (BMBF) under the KI-IoT (16ME0092) project for partly funding the work.

Data Availability Statement: Dataset available on request from the authors.

Conflicts of Interest: The authors declare no conflicts of interest.

References

1. Chou, C.C.; Lin, Z.J.; Lai, C.A.; Su, C.I.; Tseng, P.L.; Chen, W.C.; Tsai, W.C.; Chu, W.T.; Ong, T.C.; Chuang, H.; et al. A 22 nm 96KX144 RRAM macro with a self-tracking reference and a low ripple charge pump to achieve a configurable read window and a wide operating voltage range. In Proceedings of the 2020 IEEE Symposium on VLSI Circuits, Honolulu, HI, USA, 16–19 June 2020; pp. 1–2.
2. Lanza, M.; Sebastian, A.; Lu, W.D.; Le Gallo, M.; Chang, M.F.; Akinwande, D.; Puglisi, F.M.; Alshareef, H.; Liu, M.; Roldan, J.B. Memristive technologies for data storage, computation, encryption, and radio-frequency communication. *Science* **2022**, *376*, eabj9979. [CrossRef] [PubMed]
3. Gupta, V.; Kapur, S.; Saurabh, S.; Grover, A. Resistive random access memory: A review of device challenges. *IETE Tech. Rev.* **2020**, *37*, 377–390. [CrossRef]
4. Akbari, M.; Mirzakuchaki, S.; Arumí, D.; Manich, S.; Gómez-Pau, A.; Campabadal, F.; González, M.B.; Rodríguez-Montañés, R. True random number generator based on the variability of the high resistance state of RRAMs. *IEEE Access* **2023**, *11*, 66682–66693. [CrossRef]
5. Zhang, W.; Yao, P.; Gao, B.; Liu, Q.; Wu, D.; Zhang, Q.; Li, Y.; Qin, Q.; Li, J.; Zhu, Z.; et al. Edge learning using a fully integrated neuro-inspired memristor chip. *Science* **2023**, *381*, 1205–1211. [CrossRef] [PubMed]
6. Spiga, S.; Sebastian, A.; Querlioz, D.; Rajendran, B. (Eds.) *Memristive Devices for Brain-Inspired Computing: From Materials, Devices, and Circuits to Applications-Computational Memory, Deep Learning, and Spiking Neural Networks*; Woodhead Publishing: Sawston, UK, 2020; pp. xix–xx.
7. Jasmin, A.C. Filamentary model in resistive switching materials. *AIP Conf. Proc.* **2017**, *1901*, 060004.
8. Lee, J.S.; Lee, S.; Noh, T.W. Resistive switching phenomena: A review of statistical physics approaches. *Appl. Phys. Rev.* **2015**, *2*, 031303. [CrossRef]
9. Waser, R.; Menzel, S.; Rana, V. Recent progress in redox-based resistive switching. In Proceedings of the 2012 IEEE International Symposium on Circuits and Systems (ISCAS), Seoul, Republic of Korea, 20–23 May 2012; pp. 1596–1599.
10. Waser, R. Redox-based resistive switching memories. *J. Nanosci. Nanotechnol.* **2012**, *12*, 7628–7640. [CrossRef] [PubMed]
11. Dittmann, R.; Menzel, S.; Waser, R. Nanoionic memristive phenomena in metal oxides: The valence change mechanism. *Adv. Phys.* **2021**, *70*, 155–349. [CrossRef]
12. Di Martino, G.; Demetriadou, A.; Li, W.; Kos, D.; Zhu, B.; Wang, X.; de Nijs, B.; Wang, H.; MacManus-Driscoll, J.; Baumberg, J.J. Real-time in situ optical tracking of oxygen vacancy migration in memristors. *Nat. Electron.* **2020**, *3*, 687–693. [CrossRef]

13. García-Redondo, F.; López-Vallejo, M. Self-controlled multilevel writing architecture for fast training in neuromorphic RRAM applications. *Nanotechnology* **2018**, *29*, 405203. [CrossRef]
14. Wang, L.; Wang, Y.; Wen, D. Switching-enhanced RRAM for reliable synaptic simulation and multilevel data storage. *J. Alloys Compd.* **2022**, *892*, 162180. [CrossRef]
15. Ismail, M.; Mahata, C.; Kwon, O.; Kim, S. Neuromorphic synapses with high switching uniformity and multilevel memory storage enabled through a Hf-Al-O alloy for artificial intelligence. *ACS Appl. Electron. Mater.* **2022**, *4*, 1288–1300. [CrossRef]
16. Rodriguez-Fernandez, A.; Cagli, C.; Perniola, L.; Suñé, J.; Miranda, E. Effect of the voltage ramp rate on the set and reset voltages of ReRAM devices. *Microelectron. Eng.* **2017**, *178*, 61–65. [CrossRef]
17. García, H.; Vinuesa, G.; García-Ochoa, E.; Aguirre, F.L.; González, M.B.; Jiménez-Molinos, F.; Campabadal, F.; Roldán, J.B.; Miranda, E.; Dueñas, S.; et al. Effects of the voltage ramp rate on the conduction characteristics of HfO_2-based resistive switching devices. *J. Phys. D Appl. Phys.* **2023**, *56*, 365108. [CrossRef]
18. Maestro, M.; Martin-Martinez, J.; Diaz, J.; Crespo-Yepes, A.; Gonzalez, M.B.; Rodriguez, R.; Campabadal, F.; Nafría, M.; Aymerich, X. Analysis of Set and Reset mechanisms in Ni/HfO_2-based RRAM with fast ramped voltages. *Microelectron. Eng.* **2015**, *147*, 176–179. [CrossRef]
19. Fleck, K.; Böttger, U.; Waser, R.; Menzel, S. Interrelation of sweep and pulse analysis of the SET process in $SrTiO_3$ resistive switching memories. *IEEE Electron Device Lett.* **2014**, *35*, 924–926. [CrossRef]
20. Li, J.; Yang, G.; Wu, Y.; Zhang, W.; Jia, C. Asymmetric Resistive Switching Effect in Au/Nb:$SrTiO_3$ Schottky Junctions. *Phys. Status Solidi A* **2018**, *215*, 1700912. [CrossRef]
21. Wu, H.Q.; Wu, M.H.; Li, X.Y.; Bai, Y.; Deng, N.; Yu, Z.P.; Qian, H. Asymmetric resistive switching processes in W: AlOx/WOy bilayer devices. *Chin. Phys. B* **2015**, *24*, 135. [CrossRef]
22. Qin, Q.H.; Äkäslompolo, L.; Tuomisto, N.; Yao, L.; Majumdar, S.; Vijayakumar, J.; Casiraghi, A.; Inkinen, S.; Chen, B.; Zugarramurdi, A.; et al. Resistive Switching in All-Oxide Ferroelectric Tunnel Junctions with Ionic Interfaces. *Adv. Mater.* **2016**, *28*, 6852–6859. [CrossRef]
23. Jia, C.; Li, J.; Yang, G.; Chen, Y.; Zhang, W. Ferroelectric Field Effect Induced Asymmetric Resistive Switching Effect in BTiO3Nb:SrTiO3 Epitaxial Heterojunctions. *Nanoscale Res. Lett.* **2018**, *13*, 102. [CrossRef]
24. Maldonado, D.; Cantudo, A.; Perez, E.; Romero-Zaliz, R.; Perez-Bosch Quesada, E.; Mahadevaiah, M.K.; Jimenez-Molinos, F.; Wenger, C.; Roldan, J.B. TiN/Ti/HfO_2/TiN memristive devices for neuromorphic computing: From synaptic plasticity to stochastic resonance. *Front. Neurosci.* **2023**, *17*, 1271956. [CrossRef] [PubMed]
25. Pérez, E.; Zambelli, C.; Mahadevaiah, M.K.; Olivo, P.; Wenger, C. Toward Reliable Multi-Level Operation in RRAM Arrays: Improving Post-Algorithm Stability and Assessing Endurance/Data Retention. *IEEE J. Electron Devices Soc.* **2019**, *7*, 740–747. [CrossRef]
26. Pérez, E.; González Ossorio, Ó.; Dueñas, S.; Castán, H.; García, H.; Wenger, C. Programming Pulse Width Assessment for Reliable and Low-Energy Endurance Performance in Al:HfO_2-Based RRAM Arrays. *Electronics* **2020**, *9*, 864. [CrossRef]
27. Fang, R.; Chen, W.; Gao, L.; Yu, W.; Yu, S. Low-temperature characteristics of HfOx-based resistive random access memory. *IEEE Electron Device Lett.* **2015**, *36*, 567–569. [CrossRef]
28. Chiu, F.C. A review on conduction mechanisms in dielectric films. *Adv. Mater. Sci. Eng.* **2014**, *2014*, 578168. [CrossRef]
29. Lim, E.W.; Ismail, R. Conduction mechanism of valence change resistive switching memory: A survey. *Electronics* **2015**, *4*, 586–613. [CrossRef]
30. Lee, H.Y.; Chen, P.S.; Wu, T.Y.; Chen, Y.S.; Chen, F.; Wang, C.C.; Tzeng, P.J.; Lin, C.H.; Tsai, M.J.; Lien, C. HfOx Bipolar Resistive Memory with Robust Endurance Using AlCu as Buffer Electrode. *IEEE Electron Device Lett.* **2009**, *30*, 703–705.
31. Lee, H.Y.; Chen, P.S.; Wu, T.Y.; Chen, Y.S.; Chen, F.; Wang, C.C.; Tzeng, P.J.; Tsai, M.J.; Lien, C. Low-power and nanosecond switching in robust hafnium oxide resistive memory with a thin Ti cap. *IEEE Electron Device Lett.* **2010**, *31*, 44–46. [CrossRef]
32. Wang, S.Y.; Huang, C.W.; Lee, D.Y.; Tseng, T.Y.; Chang, T.C. Multilevel resistive switching in Ti/CuxO/Pt memory devices. *J. Appl. Phys.* **2010**, *108*, 114110. [CrossRef]
33. Kim, S.; Jeong, H.Y.; Choi, S.Y.; Choi, Y.K. Comprehensive modeling of resistive switching in the Al/TiOx/TiO_2/Al heterostructure based on space-charge-limited conduction. *Appl. Phys. Lett.* **2010**, *97*, 033508. [CrossRef]
34. Zeng, B.; Xu, D.; Tang, M.; Xiao, Y.; Zhou, Y.; Xiong, R.; Li, Z.; Zhou, Y. Improvement of resistive switching performances via an amorphous ZrO_2 layer formation in TiO_2-based forming-free resistive random access memory. *J. Appl. Phys.* **2014**, *116*, 124514. [CrossRef]
35. Ismail, M.; Huang, C.Y.; Panda, D.; Hung, C.J.; Tsai, T.L.; Jieng, J.H.; Lin, C.A.; Chand, U.; Anwar, M.R.; Ahmed, E.; et al. Forming-free bipolar resistive switching in nonstoichiometric ceria films. *Nanoscale Res. Lett.* **2014**, *9*, 45. [CrossRef]
36. Fang, Z.; Wang, X.P.; Sohn, J.; Bin Weng, B.; Zhang, Z.P.; Chen, Z.X.; Tang, Y.Z.; Lo, G.-Q.; Provine, J.; Wong, S.S.; et al. The Role of Ti Capping Layer in HfOx-Based RRAM Devices. *IEEE Electron Device Lett.* **2014**, *35*, 912–914. [CrossRef]
37. Gao, B.; Yu, S.; Xu, N.; Liu, L.; Sun, B.; Liu, X.; Han, R.; Kang, J.; Yu, B.; Wang, Y. Oxide-Based RRAM Switching Mechanism: A New Ion-Transport-Recombination Model. In Proceedings of the IEDM, San Francisco, CA, USA, 15–17 December 2008; pp. 1–4.
38. Dirkmann, S.; Kaiser, J.; Wenger, C.; Mussenbrock, T. Filament Growth and Resistive Switching in Hafnium Oxide MemristiveDevices. *ACS Appl. Mater. Interfaces* **2018**, *10*, 14857–14868. [CrossRef]

39. González-Cordero, G.; Pedro, M.; Martín-Martínez, J.; González, M.B.; Jiménez-Molinos, F.; Campabadal, F.; Nafría, N.; Roldán, J.B. Analysis of resistive switching processes in TiN/Ti/HfO_2/W devices to mimic electronic synapses in neuromorphic circuits. *Solid-State Electron.* **2019**, *157*, 25–33. [CrossRef]
40. Aldana, S.; García-Fernández, P.; Romero-Zaliz, R.; González, M.B.; Jiménez-Molinos, F.; Gómez-Campos, F.; Campabadal, F.; Roldán, J.B. Resistive switching in HfO_2 based valence change memories, a comprehensive 3D kinetic Monte Carlo approach. *J. Phys. D Appl. Phys.* **2020**, *53*, 225106. [CrossRef]
41. Vinuesa, G.; García, H.; Ossorio, Ó.G.; García-Ochoa, E.; González, M.B.; Kalam, K.; Kukli, K.; Tamm, A.; Campabadal, F.; Castán, H.; et al. Effect of Temperature on the Multilevel Properties and Set and Reset Transitions in HfO_2-Based Resistive Switching Devices. In Proceedings of the 2023 14th Spanish Conference on Electron Devices, Valencia, Spain, 6–8 June 2023; pp. 1–4.
42. García, H.; Dueñas, S.; Ossorio, Ó.G.; Castán, H. Current pulses to control the conductance in RRAM devices. *IEEE J. Electron Devices Soc.* **2020**, *8*, 291–296. [CrossRef]